Journal of The Electrochemical Society, 2020 **167** 090554

Transport Processes in a Li-ion Cell during an Internal Short-Circuit

Jinyong Kim, Anudeep Mallarapu, and Shriram Santhanagopalan[*,z]

Center for Integrated Mobility Sciences, National Renewable Energy Laboratory, Golden, Colorado 80401, United States of America

Internal short-circuit in a lithium-ion cell causes an abrupt increase in cell temperature and triggers subsequent thermal runaway. In this work, we present a detailed electrochemical-thermal model to investigate the physical behavior during an internal short-circuit. Simulations at wide range of heat transfer coefficients and short-circuit resistances are conducted to illustrate electrochemical and thermal behavior under a wide range of conditions. The Joule heating at the shorted region promotes electrochemical reactions nearby, causing in-plane non-uniformity of electrolyte and active material transport. Furthermore, it is found that diffusion in solid active materials plays a significant role at very high shorting currents (~20 C), as electrochemical reactions rate are being controlled progressively more by availability of Li^+ at the interface, due to limitations in diffusion through the active material with increasing discharge rates. This diffusion limitation causes a drop in available energy, and subsequently a decrease in cell equilibrium potential and the heat generation rate at the location of the short. On the other hand, rapid depletion of lithium concentration in the electrolyte and accumulation on the electrode surface results in highly non-uniform transport properties resulting in higher heat generation rates. Hence, the heating regime shifts from "local heating" to "global heating". Based on the findings, important design parameters for battery safety are discussed.

 [DOI: 10.1149/1945-7111/ab995d]

Manuscript submitted February 14, 2020; revised manuscript received May 7, 2020. Published June 16, 2020. *This paper is part of the JES Focus Issue on Battery Safety, Reliability and Mitigation.*

Supplementary material for this article is available online

Lithium-ion batteries (LIB) are considered as one of the most promising candidates for the energy source of next-generation vehicles owing to their high energy density, high round-trip efficiency and no memory effect.[1] However, the safety of LIBs is still a primary concern for the commercialization of electric vehicles (EV). Owing to increasing market share of EVs, number of incidents being reported, such as fire and venting , is gradually increasing, which raises more public concern to EV technologies. Safety of EV is strongly affected by heat transport process. When a local temperature in a cell exceeds a threshold value (120 °C–200 °C), exothermic abusive reactions[2,3] and corresponding internal volatile gas build-up[4–6] take place, which attributes the detrimental consequences such as battery thermal runaway.[5,7–9] To prevent such hazardous events, it is imperative to elucidate the physical process that initially triggers such increase of local temperature to the threshold value.

Internal short-circuit (ISC) is one of the physical processes that triggers thermal runaway of battery packs and is believed one of the most serious safety concerns to the LIB technology. ISC can be caused by many factors such as material impurities,[10] nail penetrations[11] and mechanical deformations,[12] as described in Fig. 1a. During ISC, large amount of current is passing through the shorted region, causing large amount of Joule heating at the shorted region. The generated heat at the shorted spot is then dissipated to the surrounding region, causing the damage propagation along in-plane direction. On the other hand, the current passing through the shorted region is generated by electrochemical reactions of active materials, which involves transport of electrolyte and currents in the damaged cell along through-plane direction. Therefore, physical processes during ISC are inherently multi-dimensional and understanding multi-dimensional aspects of transport processes is therefore the key to achievement of battery safety and hence mainstream adoption of EVs. Numerical modeling is an effective approach to understand such physical processes, and a successful numerical model needs to consider multi-dimensional aspects of both thermal and electrochemical behaviors, in order to correctly capture important physics associated with ISC.

Several modeling efforts are reported to study electrochemical and thermal behaviors under ISC conditions. Simplified electrochemical models,[12–15] such as equivalent circuit models[12–14] and single-particle models[15] are adopted to simulate short-circuit behaviors under mechanical deformations. To capture the Joule heat generated by local short-circuit, customized local short-circuit resistance is added, which is correlated to the local mechanical strain.[12] Detailed models that solve sets of partial differential equations, such as pseudo two-dimension (P2D) models, are also utilized to simulate physical behaviors during ISC.[10,11,16–19] Zhao et al.[11,16] demonstrates time evolutions of three-dimensional (3D) temperature and voltage fields during nail penetrations[11] and internal short-circuits[16] of pouch cells, using a commercial software package, Autolion™.[20] It is found that two regimes, "global heating" and "local heating," exist and the transition of the regime depend on the ratio of internal cell resistance and the short resistance,[11] while Fang et al.[17] also demonstrate a similar trend. Santhanagopalan et al.[19] investigate thermal response of a cylindrical cell under different short-circuit scenarios using a detailed multi-dimensional thermal-electrochemical model, while a similar study is conducted by Zavalis et al.[10] for a simplified cubic cell. However, there is still a lack of information in the literature reported so far, such as (i) multi-dimensional distributions of active material, (ii) multi-dimensional transport of liquid electrolyte and (iii) voltage response depending on different heat transfer conditions. These are vital to understanding the physical process during ISC and therefore must be illustrated by numerical framework.

In this work, we present a coupled two-dimensional (2D) electrochemical-thermal model to elucidate the underlying physical mechanisms associated with the internal short-circuit processes of LIBs. Special attention ispaid to transport processes and in-plane distributions of key properties. A series of simulations are conducted at wide range of heat transfer coefficients and short-circuit resistances, to explore their effects on voltage and temperature responses at wide range of conditions. Furthermore, by varying electrochemical parameters, we discuss the role of different transport processes during ISC and reveal that the diffusion of active material is one of

*Electrochemical Society Member.
[z]E-mail: Shriram.Santhanagopalan@nrel.gov

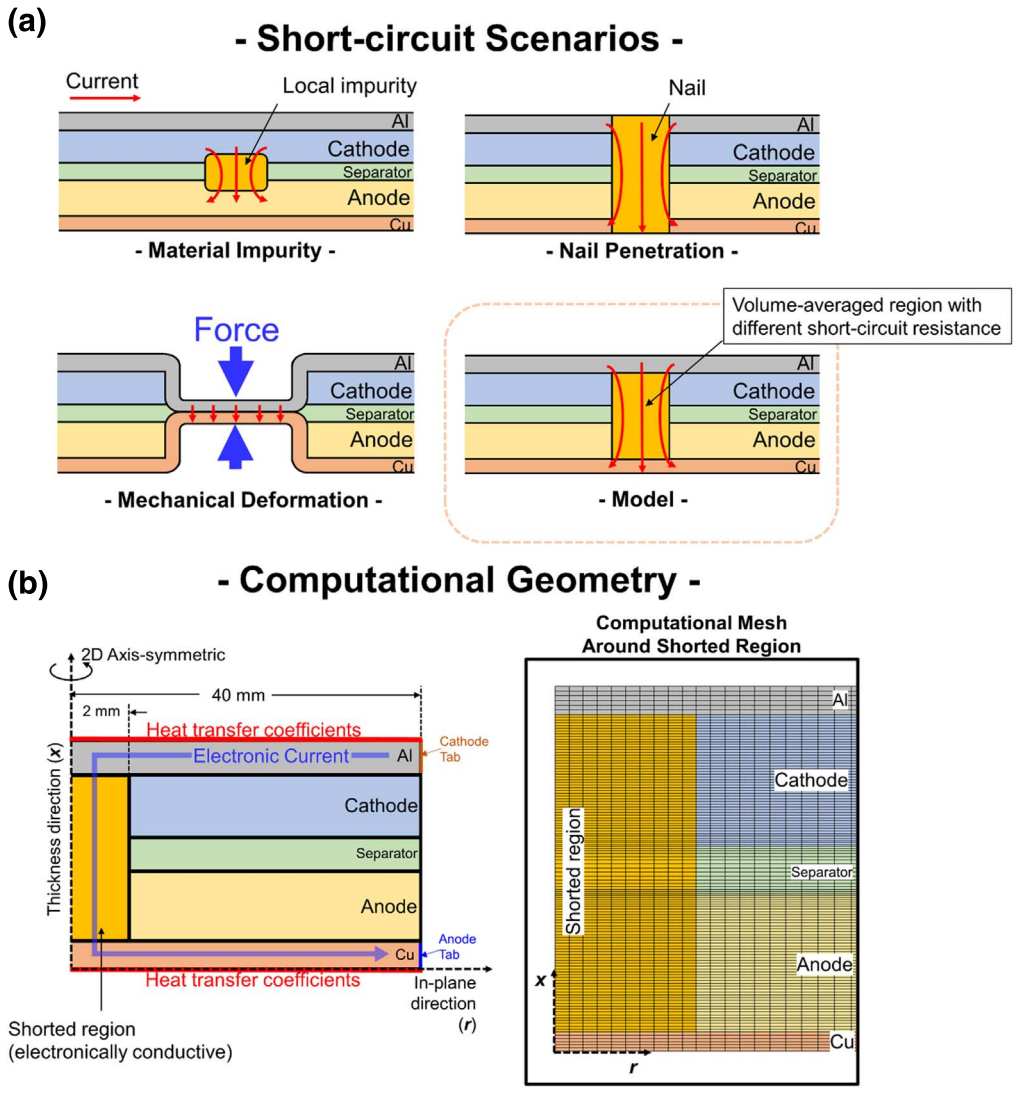

Figure 1. (a) Types of short-circuit scenarios (b) Schematic description of computational geometry and computational mesh around the shorted region.

the most important factors contributing the temperature increase at initial stage at very severe shorting conditions.

Numerical Model

Governing equations.—The current numerical model solves following governing equations:

- Charge conservation in solid electrodes, current collectors and short-circuit region:

$$0 = \nabla \cdot (\sigma^{eff} \nabla \phi_s) - j^{Li} \quad [1]$$

- Charge conservation in electrolyte:

$$0 = \nabla \cdot (\kappa^{eff} \nabla \phi_e) + \nabla \cdot (\kappa_D{}^{eff} \nabla \ln c_e) + j^{Li} \quad [2]$$

- Species conservation in electrolyte:

$$\frac{\partial(\epsilon_e c_e)}{\partial t} = \nabla \cdot (D_e{}^{eff} \nabla c_e) + \frac{1 - t_+{}^0}{F} j^{Li} \quad [3]$$

- Species conservation in active material particles (parabolic approximation):

$$\frac{\partial(\epsilon_s c_s)}{\partial t} = -\frac{j^{Li}}{F} \quad [4]$$

$$D_s \frac{\overline{c_s} - c_{s,surf}}{l_{se}} = \frac{j^{Li}}{a_s F} \quad [5]$$

- Energy conservation

$$\frac{\partial(\rho c_p T)}{\partial t} = \nabla \cdot (k_{eff} \nabla T) + \dot{q}_{irrev} + \dot{q}_{Joule} \quad [6]$$

The current numerical model is based on the work by Gu and Wang,[21] Smith and Wang[22] and Doyle et al.[23] Therefore a detailed description of these governing equations is not repeated here. Reversible entropic heat, which accounts for 5%–10% of total heat budget,[24] is neglected in this analysis. The parabolic approximation[21] is used to evaluate the surface concentration of active materials owing to its simplicity and computational efficiency. However, note that this approximation may cause inaccuracies, especially at the initial stage, due to the high short-circuit current condition in this study.[22]

While the detailed current path or heat path can vary under different short-circuit scenarios, it is difficult to develop explicit representation of the electrical pathways even for a given scenario. However, the different shorts do have similarities in that the electronic current flows from cathode current collectors to anode current collectors, the heat is generated near the short region and dissipated away from the short. Based on these observations, the short-circuit is modeled by adding a shorted zone as seen in Fig. 1, which is a volume-averaged representation of the geometry around the short. Equations 1 and 6 are solved in the shorted zone, as the shorted zone is electronically conductive. As discussed earlier, an internal short-circuit can be attributed to different causes. Accordingly, the current passing through the shorted zone can be different depending on the electronic resistance. If the electronic resistance of a shorted region is known, the short-circuit current (Eq. 7) and the corresponding Joule heat (Eq. 8) assuming uniform voltage at current collectors can be expressed as:

$$I_{SC} = \frac{\phi_s|_{ca,cc} - \phi_s|_{an,cc}}{R_{SC}} \quad [7]$$

$$Q_{SC} = {I_{SC}}^2 R_{SC} \quad [8]$$

The short-circuit current between cathode current collector and anode current collector, through the shorted region, is considered in this study. Typically, the electronic conductivity of the current collectors are 3–4 orders of magnitude higher than that of electrodes. As a consequence, the electronic current between the active material and the short-circuit region is negligible, compared to that between the current collectors through the shorted region. In that case, the evaluation of the short-circuit resistance is greatly simplified as $R_{SC} = L_{SC}/(\sigma_{SC}\pi {r_{SC}}^2)$ for the geometry shown in Fig. 1.

The short-circuit resistance does by vary depending on the type of short-circuit scenario. For example, a case with local small material impurities can be considered high resistance short-circuit (small short-circuit current) that may burn out with time, and a case with a nail penetration or large deformations can lead to small values for the short-circuit resistance (large short-circuit current). In order to calibrate the short-circuit resistance, separate experiments are conducted to measure the voltage drop across an electrode sandwich and the electronic conductivity of the shorted region, σ_{SC}, is varied according to experimentally measured voltage drop across the sandwich.

Initial and boundary conditions.—There are several boundary conditions we need to define in the current geometry. *Supplementary Material I* describes these simulation conditions in detail.

- *Initial conditions*

At the beginning of the simulation, the electrolyte concentration and the active material concentration of anode and cathode are prescribed as:

$$c_e = c_{e,0} \quad [9]$$

$$c_{s,k} = c_{s,k,0} \quad [10]$$

where the suffix $k = c$ represents the cathode and $k = n$ represents the anode. The initial electrode potentials at anode and cathode are also prescribed as:

$$\phi_{s,a} = 0,\ \phi_{s,c} = U_{eq,c}(x_{ca,0}) - U_{eq,a}(x_{an,0}) \quad [11]$$

The electrolyte potential at both the anode and cathode is consistently set as follows to describe the fact that the solution phase and the electrodes are in electrochemical equilibrium; i.e., $\phi_{s,0} - \phi_{e,0} = U_{eq}(x_0)$:

$$\phi_{e,0} = -U_{eq,a}(x_{an,0}) \quad [12]$$

- *Boundary conditions: Electrolytes*

As the electrolyte can only exists inside porous matrix of electrodes and separator. Hence, zero-flux boundary conditions are set for the Eqs. 2 and 3 at the interfaces between porous zones (electrodes and porous zones) and other parts as:

$$\left.\frac{\partial \phi_e}{\partial n}\right|_{outer\ porous\ zone} = 0,\ \left.\frac{\partial c_e}{\partial n}\right|_{outer\ porous\ zone} = 0 \quad [13]$$

The location of each boundary condition is described in Supplementary Material I.

- *Boundary conditions: Solid potentials*

The voltage at the outer edge ($r = R_{cell}$) of the anode current collector is set to zero as a Ref. 25.

$$\phi_s|_{an,cc,r=R_{cell}} = 0 \quad [14]$$

No-flux boundary conditions are specified at the outer edge of the cathode current collector since there is no external load current considered in this work (i.e., $I_{app} = 0$).

$$\left.\frac{\partial \phi_s}{\partial n}\right|_{ca,cc,r=R_{cell}} = 0 \quad [15]$$

All current flow across the boundaries of the separator is ionic. Therefore, zero-flux boundary condition is set at the surface that encompasses the separator:

$$\left.\frac{\partial \phi_s}{\partial n}\right|_{sep,outer\ surfaces} = 0 \quad [16]$$

At all the other boundary surfaces, zero flux conditions are prescribed.

- *Boundary conditions: Temperature*

Heat transfer away from the cell is an important factor that influences the outcome of a short-circuit event. To mimic different cooling conditions, we conducted a parametric sweep of the heat transfer coefficients set at the current collector surfaces over a wide range:

$$q''|_{an,cc\ \&\ ca,cc} = -h(T - T_\infty) \quad [17]$$

where the far-field temperature (T_∞) of 300 K was specified. At all the other boundary surfaces, zero flux conditions are prescribed.

Numerical methods.—Figure 2 shows a flow chart of the simulation procedure. The governing equations are discretized and solved using the commercial computational-fluid dynamics (CFD) software Ansys Fluent® (Version 19.2).[26] In order to implement customized equations, properties and source terms, user-defined functions (UDF) with three additional user-defined scalars (UDS) are added. These three UDSs are solved sequentially until the solution criteria are met. In all the simulation cases, the convergence criterion is set to 0.1% for the species (electrolyte concentration) and charge balance. A first-order implicit scheme is used for the time marching due to its numerical stability.

Special attention is paid to the numerical stability owing to very high discharge rates. As we use CFD approach based on

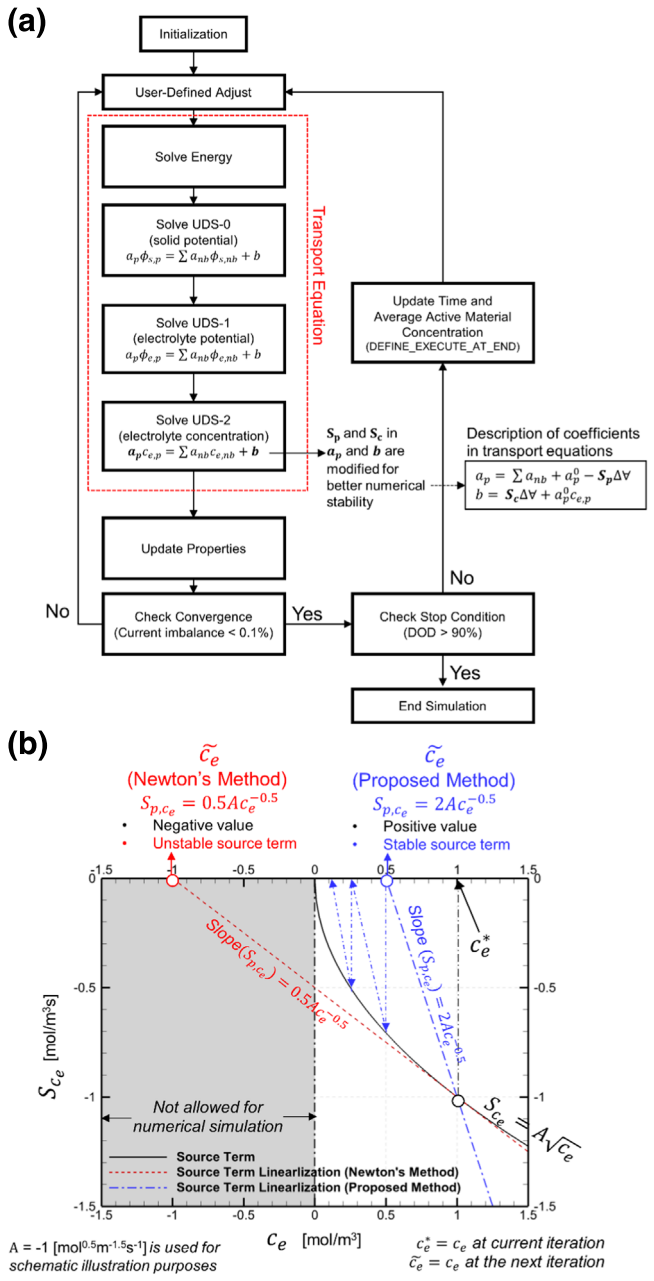

Figure 2. (a) Flow chart of simulation procedure[26] (b) Schematic description of source term linearization for the electrolyte transport equation following the procedure outlined in Ref. 27.

finite-volume method (FVM) to solve discretized equations, appropriate treatment of source terms is crucial to the numerical stability. Usually, numerical stability issues arise when solving the species conservation equation of electrolyte (Eq. 3).

In the current work, the source term (the last term on the right hand side of Eq. 3) is linearized using the method outlined by Patanker[27] as follows:

$$S_{c_e} = S_{C,c_e} + S_{P,c_e} c_{e,p} \qquad [18]$$

where S_{C,c_e} is a constant part of the source term and S_{P,c_e} is a coefficient for $c_{e,p}$. It is often desired to select the coefficient, S_{P,c_e}, to be $\partial S_{c_e}/\partial c_{e,p}$, which corresponds to Newton's method.[27] However, physically constraints dictate that Li^+ concentration in the electrolyte is always positive and therefore the numerically calculated electrolyte concentration should also always remain positive during the iterations. To achieve good numerical robustness, the solution of the discretized form of Eq. 3 should maintain positive values for c_e even under extremely high current conditions. These are categorized by Patankar[27] as source term dominant conditions, for which the discretized equation (Eq. 18) is then reduced to:

$$S_{C,c_e} + S_{P,c_e} c_e \approx 0 \qquad [19]$$

upon convergence. The background for this numerical implementation is already discussed in Ref. 27, and we next, apply this method to the present numerical framework.

The source term on Eq. 3 is expressed as:

$$\begin{aligned} S_{c_e} &= \frac{1 - {t_+}^0}{F} j_{Li^+} \\ &= \underbrace{\sqrt{c_e}\sqrt{c_{s,surf}(c_{s,\max} - c_{s,surf})}\, a_s k_0 \sinh\left(\frac{\alpha F}{RT}\eta\right)}_{A_{c_e}} \times \frac{1 - {t_+}^0}{F} \\ &= A_{c_e}\sqrt{c_e} \end{aligned} \qquad [20]$$

Figure 2b shows the schematic description of the source term linearization method in the present work. For the sake of illustration, if we assume $A_{c_e} = -1[\text{mol}^{0.5}\text{m}^{-1.5}\text{s}^{-1}]$ and initial $c_e{}^* = 1[\text{mol} - \text{m}^{-3}]$, one can select the slope S_{P,c_e} based on Newton's method to be $A_{c_e}/(2\sqrt{c^*_e})$, which represents $\partial S/\partial c_e$, and the corresponding S_{C,c_e} is:.

$$S_{C,c_e} = S_{c_e} - S_{P,c_e} c_e{}^* = \frac{A_{c_e}}{2}\sqrt{c_e{}^*} \qquad [21]$$

The value of c_e at the next iteration ($\tilde{c_e}$), is then given by[27] $-S_{C,c_e}/S_{P,c_e} = -\tilde{c_e}$. This results in a negative value for c_e at the next iteration. (see also Eq. 19 and Fig. 2b). The consequence of this treatment is the numerical blow-up of the source term because the square root function in the source term does not accept negative input values.

This can be alleviated by adjusting the slope S_{P,c_e} to be such that c_e is positive in the next iteration. For instance, if the slope $S_{P,c_e} = 2/\sqrt{c_e{}^*}$, then the corresponding S_{C,c_e} is:

$$S_{C,c_e} = S_{c_e} - S_{P,c_e} c_e = -A_{c_e}\sqrt{c_e{}^*} \qquad [22]$$

This results in the $\tilde{c_e}$ (c_e at next iteration) to be $-S_{C,c_e}/S_{P,c_e} = \tilde{c_e}/2$. This has the same sign as the value of c_e at the current iteration ($c_e{}^*$), and therefore the solution remains always positive under this modified treatment (see Fig. 2b). Another implication of this treatment is that the value of $c_e{}^*$ decreases by half at each iteration and eventually reaches the converged value specified by the tolerance criterion, which satisfies Eq. 19. One may argue that choosing $S_{P,c_e} = 1/\sqrt{c_e}$ results in convergence at the first iteration, and hence would be more effective. However, such an abrupt change in the value of c_e causes numerical oscillations when solving for other variables. Note that the slope, S_{P,c_e}, is a variable chosen by the user and an increase in the magnitude of the slope usually results in a slowdown of the convergence.[27] In this work, we choose $S_{P,c_e} = 2/\sqrt{c_e{}^*}$.

For the charge conservation equations within the electrodes and the electrolyte, S_P values are chosen as follows:

$$\begin{aligned} S_{P,\phi_s} &= \frac{\partial S_{\phi_s}}{\partial \phi_s} = \frac{\partial S_{\phi_s}}{\partial \eta}\frac{\partial \eta}{\partial \phi_s} \\ &= -\sqrt{c_{s,surf}\, c_e (c_{s,\max} - c_{s,surf})}\, a_s k_0 \cosh\left(\frac{\alpha F}{RT}\eta\right) \end{aligned} \qquad [23]$$

$$S_{P,\phi_e} = \frac{\partial S_{\phi_e}}{\partial \phi_e} = \frac{\partial S_{\phi_e}}{\partial \eta}\frac{\partial \eta}{\partial \phi_e} = -\sqrt{c_{s,surf}\, c_e (c_{s,\,\max} - c_{s,surf})}\, a_s k_0 \cosh\left(\frac{\alpha F}{RT}\eta\right) \quad [24]$$

where the overpotential is defined as $\eta = \phi_s - \phi_e - U_{eq}(x_{surf})$. Note that the coefficients, S_P, are equal in Eqs. 26 and 27, since $S_{\phi_s} = -S_{\phi_e}$ in our model equations.

Before presenting detailed results, the current numerical model is first validated by comparing the profiles against values reported in the open literature. 1D numerical results from Rahimian et al.[25] are selected as a validation target for current numerical model as all parameters[28,29] are well-organized and documented in this work. Parameters, schematic of 1D geometry and comparisons of discharge curves are shown in Table SI, Fig. S1 and Fig. S2 in Supplementary Material II (available online at stacks.iop.org/JES/167/090554/mmedia), respectively. As seen in the figure, current model shows good agreement against the model by Rahimian et al.[25] Note that the current model uses the parabolic assumption for the active materials, while Rahimian et al.[25] use the pseudo-2D (P2D) model. A series of short-circuit simulations are then conducted after the successful validation of the current numerical model.

Figure 1 shows numerical domains used in the current study. Figure 1a shows the schematic of the short-circuit problem to be solved and Fig. 1b shows the actual numerical domain. As described in the figure, the domain consists of current collectors, negative electrodes, positive electrodes, separators, and short-circuit regions. We use an idealized axis-symmetric geometry with an internal short-circuit at the middle of the cell for illustration of the numerical approach. In this model, the short-circuit is represented using a volume averaged short circuit resistance that is considered to be uniform. This assumption is valid for a nail penetration case, since Zhao et al.[11] pointed out that the nail penetration process is very quick (<1 s) considering the typical thickness of cell (1 ~ 2 cm) and the nail penetration speed (8 cm s^{-1}). However, this will not be valid for the material impurity case, since a heterogeneity in short-circuit resistance along the thickness direction is expected for the latter case. More elaborate representations of the short circuit that consider the nature of the short[19] or various explicit circuits to model the electrical pathways[6] have been proposed earlier. Knowing the detailed mechanism of short circuit, equivalent representations using a lumped resistance similar to Eq. 7 can be proposed. The diameter of the shorted zone and the cell are chosen to be 4 mm and 80 mm, respectively, based on the modeling work by Zhao et al.[11] who simulated the evolution of physical states under nail penetration. The nail diameter and the cell dimensions used in Zhao et al.[12] are 4 mm and 80 mm × 130 mm × 2.6 mm, respectively. In the current work, the cell capacity per layer is 0.1 Ah, while this is 0.19 Ah in the work by Zhao et al.[11], owing to approximately twice larger geometric area of the electrodes. Note that this simple axis-symmetric geometry is chosen to more clearly elucidate the physics around the shorted region by simplifying the problem (the number of computational nodes = 13414), whereas this numerical framework scales readily to 3D cell geometries. Another important point to note is that unlike other previous implementations[26,30] the electrochemical and thermal simulations are conducted on the same numerical grid. In other words, implementation of the numerical scheme presented here improves computational efficiency considerably that the electrochemical model can be solved on the actual geometry.

Physical and geometrical parameters summarized in Table I and Table II are from Rahimian et al.[25] with two major exceptions: (i) the Bruggeman coefficient of the anode electrode reported in Ref. 25 is too high (4.1) that this prevents complete discharge under very high currents and (ii) the diffusivity of cathode solid-phase diffusion coefficient listed in Ref. 25 is several orders of magnitude higher (10^{-11} m^2 s^{-1}) than conventionally reported values (~$10^{-13\sim14}$ m^2 s^{-1}). The thermal and electrical properties are from Zhao et al.[11] Additional details are listed in Tables I and II.

In order to quickly design the target cooling rates for short-circuit conditions, one may use a global heat balance equation to choose effective heat transfer coefficients at the surfaces of batteries. If one wishes to control the average temperature to be lower than a desired maximum temperature, the condition listed below should be satisfied:

$$hA_{cell}(T_{\max} - T_\infty) > \dot{q} \quad [25]$$

Assuming that Joule heating at the shorted region is the dominant mechanism, heat generation rate can be expressed as $\dot{q} = V^2{}_{cell}/R_{SC}$. Based on prior work,[11,17] it is estimated that the discharge currents at a very low resistance shorting condition is in the range of 10C–20C, which should be same as the current passing through the shorted region ($I_{SC} = V_{Cell}/R_{SC}$) due to charge conservation. In this work, we choose $I_{SC} = 15$C and $T_{\max} = 100$ °C to design the baseline condition, which corresponds to $R_{SC} = 2.5\Omega$ and $h = 8$ Wm^{-2} K^{-1} assuming $V_{cell} = 4$ V. Next, a wide range of simulations are conducted by varying to R_{SC} and h. Note that same heat transfer coefficients are set at both anode and cathode current collector surfaces.

Results and Discussion

This section shows an overview of numerical results evaluated from the current model and provides the cell voltage and temperature

Table I. Physical Parameter (*ad: adjusted).

Parameter	Positive Electrode	Separator	Negative Electrode	References
Initial porosity, ϵ	0.4382	0.45	0.3	25
Bruggeman factor, p	1.5	1.5	1.5	*ad
Diffusivity of solid active material, D_s (m^2 s^{-1})	1.0E-14[*ad]	–	5.5E-14[25]	–
E_a(Diffusivity of solid active material)	20000	–	4000	21
Maximum concentration of solid active materials, $c_{s,\,\max}$ (mol m^{-3})	30555	–	51555	25
Initial stoichiometry of solid active materials, $x_{100\%}$	0.465	–	0.756	25
Particle radius, R_s (μm)	12.5	–	8.5	25
Rate constant for electrochemical reactions, k_0 ($m^{2.5}mol^{-0.5}$ s^{-1})	2.0E-11		5.0E-11	*ad
E_a (Rate constant, J mol^{-1})	20000		20000	*ad
Equilibrium potentials, U_{eq} [V]	Ramadass et al.[29]			
Lithium ion transference number in the electrolyte, t_0^+ [−]	0.435			25
Thermodynamic factor, $\partial ln f_\pm / \partial ln c_e$; [−]	0			25
Initial electrolyte concentration, $c_{e,0}$ (mol m^{-3})	1000			25
Electrolyte diffusivity, D_e (m^2/s)	Valøen and Reimers[28]			
Electrolyte conductivity, κ (S m^{-1})	Valøen and Reimers[28]			

Table II. Geometric and Thermal Parameter (*ad: adjusted).

Parameter	Al Foil	Positive Electrode	Separator	Negative Electrode	Cu Foil	References
Thickness, δ [μm]	15^{*ad}	73.5	25	70	10^{*ad}	25
Heat conductivity, k [W/m-K]	240	0.4	0.5	0.4	395	11
Density, ρ [kg m^{-3}]	2700	2860	525	1200	8960	11
Heat capacity, c_p [J/kg-K]	897	1150	2050	1150	385	11
Electronic conductivity, σ [S m^{-1}]	6.0×10^7	10	—	100	3.8×10^7	21

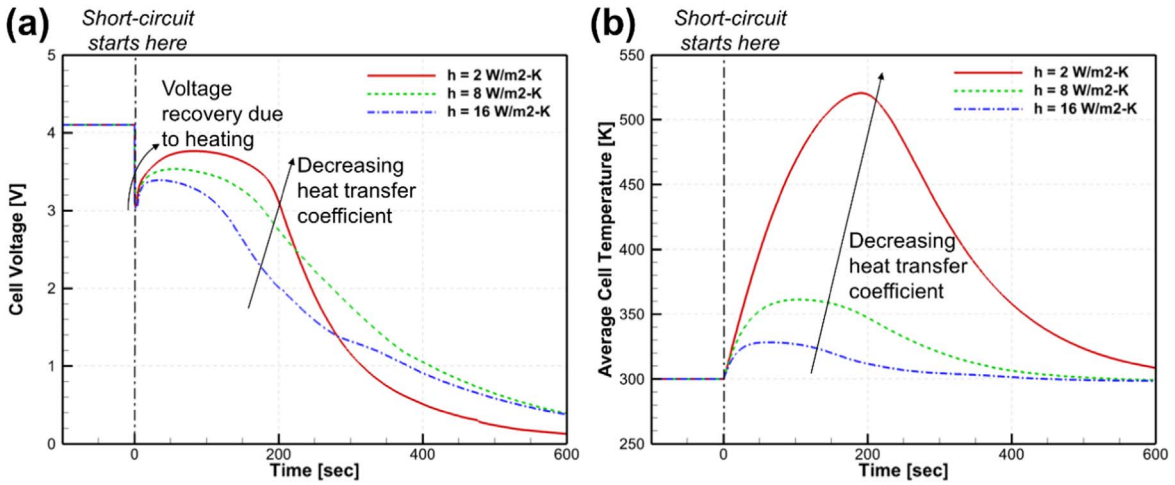

Figure 3. (a) Cell voltage and (b) average cell temperature responses vs various heat transfer coefficients ($R_{SC} = 2.5\Omega$).

responses vs various cooling rates by setting different heat transfer coefficients at the surface of the current collectors.

Voltage and temperature response vs heat transfer coefficients.—Temperature affects the electrochemical behavior of LIBs and usually higher temperature results in better electrochemical kinetics. As seen in Fig. 3a, using lower heat transfer coefficients (lower cooling rate) results in higher cell voltage after the short (i.e., more voltage recovery immediately following the short circuit). This is due to higher local temperatures along this timeline as shown in Fig. 3b. Once the temperature rise subsides, this trend in voltage recovery tends to even out. These results indicate that the voltage trends from short-circuit tests can be used to design cooling rates for cells, since a higher voltage recovery (defined as the difference between maximum voltage and the voltage at t = 0_+sec) during short-circuit events represents a poorer heat management system. The case with $h = 2$ Wm^{-2} K^{-1} shows maximum average cell temperature of 520 K (247 °C) at 195 s, which implies that the cell is likely to experience a thermal runaway as the temperature is higher than 120 °C, which is commonly used as the onset temperature to a thermal runaway. Cases with $h = 8$ Wm^{-2} K^{-1} and $h = 16$ Wm^{-2} K^{-1} show a maximum average cell temperature of 360 K (87 °C) and 325 K (52 °C), respectively. Although these average cell temperatures are less than the onset temperature, it is important to also observe the local temperature fields since the local temperature can be higher than the onset temperature.

Figure 4a shows the time evolution of radial distributions of temperature for $h = 8$ Wm^{-2} K^{-1} during a localized short-circuit. At the initial stage (t = 12 s), a rapid temperature increase around the shorted region is observed due to the large Joule heating at the shorted region. At t = 112 s, where the average cell temperature reaches its maximum value (360 K, Fig. 3b), the maximum local temperature is much higher at 560 K (287 °C), which indicates that the cell is susceptible to thermal runaway, triggered at the shorted region. Owing to the higher temperature around the shorted region at the initial stage, more current is also being generated around the shorted region due to faster kinetics as seen in Fig. 4b. At the initial stage (t = 12 s), the current density around the shorted region (720 A m^{-2}) is roughly three times higher than the current density at the boundaries far from the short-circuit (200 A m^{-2}). Subsequently, though, the distribution of the current density across the electrode evens out due to relaxation of the ion distribution in the solution phase. These results are in tune with experimentally observed[17] profiles for the voltage drop following a short circuit: there is a significant drop in potential for the first few seconds, following which the voltage tapers off gradually.

As a result, the active material is depleted much faster around the shorted region as described in Fig. 5. Figures 5a–5b describe the contour of Li^+ concentrations within the active material at 12 and 112 s respectively. First, active material is being depleted much faster near the shorted region, which is mainly attributed to the temperature effect shown in Fig. 4. Second, the concentration of active material is more uniform in the thickness direction near the shorted region. This is also attributed to the higher temperature, as hotter region has faster kinetics. Figure 5c shows radial distribution of active material at various time, which also indicates that active material is depleting faster around the shorted region. It is worth pointing out that the maximum gradient in concentration across the electrode correlates well with the temperature profiles shown on Fig. 3b.

The discharging process is often limited by the transport of Li^+ in liquid electrolyte. Hence, it is important to observe the response of the liquid electrolyte for better understanding of the short-circuit process. Figure 6 describes the distribution of Li^+ concentration in liquid electrolyte, along with the flux for the same instances of time shown on Fig. 5. The flux of Li^+ in liquid electrolyte is expressed as:

$$\vec{j}_{c_e} = -D_{c_e}^{eff} \nabla c_e \qquad [26]$$

At the initial stage (t = 12 s) (Fig. 6a), Li^+ is being depleted from the active material much faster near the cathode current collector-short-region interface. This is due to the expedited diffusion of Li^+

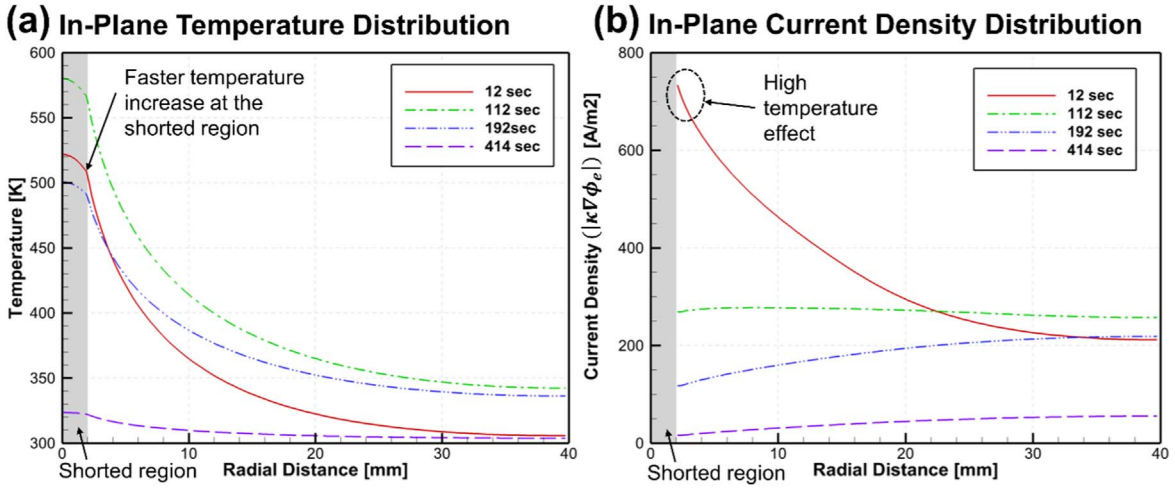

Figure 4. Time evolution of (a) radial distributions of temperature (b) current density at the mid-separator.

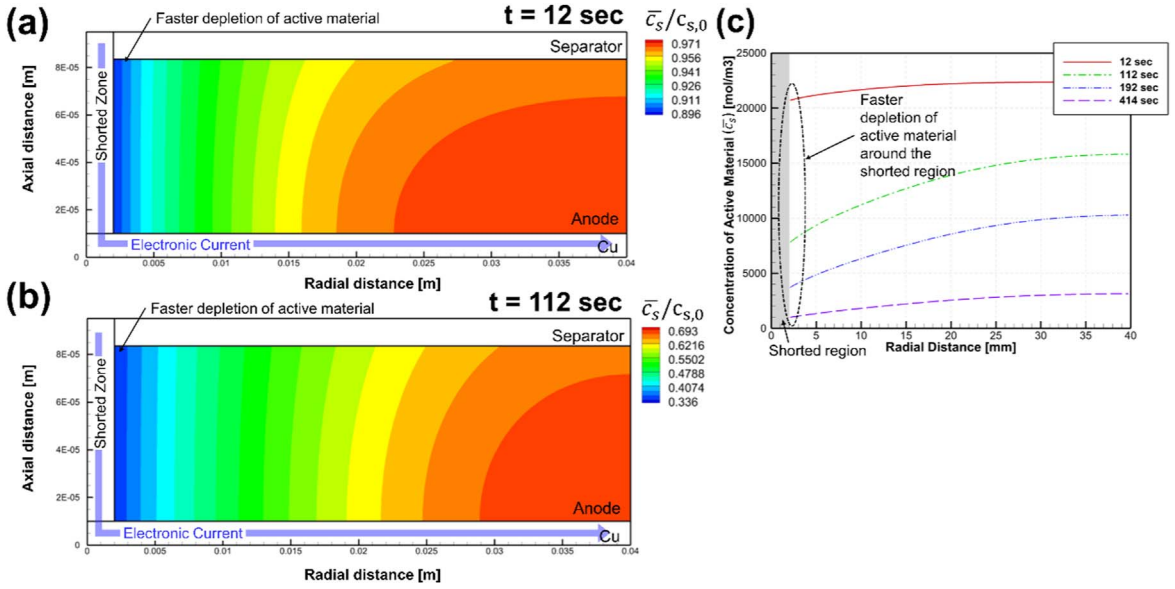

Figure 5. Distribution of active material concentration in anode at (a) 12 s and (b) 112 s. (c) Radial distribution of active material in mid-anode at various time.

into the active material at that interface, promoted by the higher temperatures and resultant current densities as shown in Fig. 4 and proximity to the electron source. A mirror effect is noticed at the interface between the anode current collector and the short-circuit region. In this case, the Li^+ concentration in the electrolyte readily increases due to rapid discharge of the anode near this interface. As it can be seen in Fig. 6b, the electrolyte depletion near the short circuit recovers at t = 112 s and the electrolyte concentration at the cathode region is as high as 700 mol-m^{-3}. Also, the flux of Li^+ at the separator becomes relatively more uniform, compared to the case at 12 s. However, non-uniformity in electrolyte concentrations far from the short-region persist for longer periods of time, resulting in slow but persistent heat up of the cell (See Fig. 9).

Voltage and temperature responses vs short-circuit resistances.—Figure 7 shows variations in key metrics at various internal short-circuit resistances. Figure 7a shows voltage responses at different short-circuit resistances. Two important phenomena are observed in Fig. 7a. First, a larger voltage drop is observed with decreasing short-circuit resistance due to higher discharging current. More interestingly, the voltage recovery gradually increases with decreasing short-circuit resistances until it reaches its maximum value at $R_{SC} = 1.25\Omega$. This corresponds to the heat generation rate is also the highest at $R_{SC} = 1.25\Omega$ as seen in Fig. 7c. However, the voltage recovery decreases with decreasing short-circuit resistance and it is almost negligible in cases with $R_{SC} = 0.31\Omega$ and $R_{SC} = 0.16\Omega$. For these cases, drop in cell voltage due to the thermodynamic inability of the active material to hold back the Li^+ outweighs improvements to transport properties due to the temperature rise.

As it is found that the voltage recovery is related to thermal condition, Fig. 7b shows the evolution of temperature at different short-circuit resistances. It is seen that the maximum average temperature increases with decreasing short-circuit resistance until $R_{SC} = 1.25\Omega$, where it shows its highest value (365 K), and then it decreases with decreasing short-circuit resistance when $R_{SC} < 1.25\Omega$. To investigate underlying reasons, a budget analysis for heat generation rates is conducted at different short-circuit resistances (at 90% SOC or 4 V). It is found that the trend in temperatures can be mainly attributed to the decrease of joule heat generation rate at short-circuit region, past the 1.25 Ω case, while the internal cell heat generation rate due to discharging ($Q_{cell,\text{internal}}$) gradually increases with decreasing R_{SC} (See Fig. 7c). Also, as the fraction of heat generation at the shorted region gradually decreases with decreasing

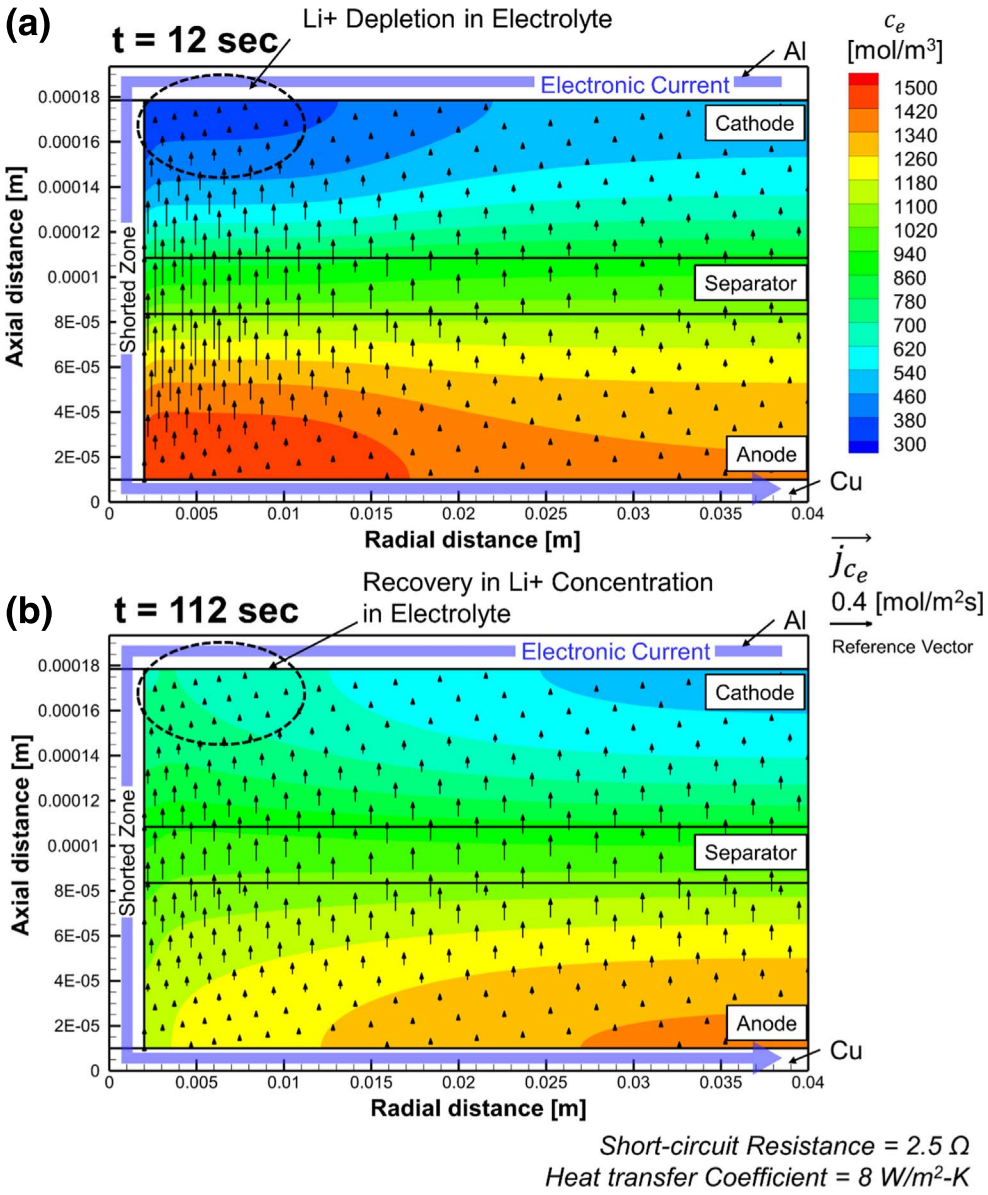

Figure 6. Time evolution of Li+ concentration in electrolyte and diffusion flux of Li+ in electrolyte at (a) 12 s, (b) 112 s.

short-circuit resistance, the heating regime gradually shifts from "local heating" regime to "global heating" regime, while similar trends are observed in Refs. 11, 17, 30. It is this trend in heat generation that results in the relative variation in electrolyte concentrations at the region close to the short, vs those far away from the short as shown in Fig. 6. Changes in availability of Li^+ subsequently determines the potential for transformation of a localized short-circuit to global heating of the cell. In cases where there are no significant transport limitations, the concentration profiles are much more uniform and result in a global short. The magnitude of heat generated for this case is higher. However, for the case with higher transport limitations (similar to results shown in Fig. 6) the maximum heat generation rate is lower; however, the duration of the short is longer.

The change in cell internal heat generation ($Q_{cell,\text{internal}}$) seems to originate from limitations to diffusion within the solid particles. Figure 7d shows the variation of discharging C-rate (at 90% SOC) with various short-circuit resistances. As the short-circuit resistance decreases, the discharging C-rate increases and converges to roughly 20C for the parameter set chosen for this study. Also, the effective cell equilibrium potential gradually decreases and levels off at roughly 1.0 V as the short-circuit resistance decreases. Based on the equivalent circuit model outlined in Refs. 17, 30, the effective cell equilibrium potential is given by following formula:

$$U_{eq} = V_{cell} + IR_{cell} = V_{cell} + \frac{Q_{cell,\text{internal}}}{I} \quad [27]$$

According to the simple circuit model discussed in Refs. 17, 30, the total heat generation rate is strongly affected by equilibrium potential, as total heat generation rate is proportional to the square of the equilibrium potential. The important point to note is that the equilibrium potential is only meaningful at the interface between the electrolyte and the active material, which is highly dependent on the local current density. For example, at high discharge rates, the concentration of cathode active material at the surface is significantly larger than its volume-averaged value, resulting in a much lower equilibrium potential. When the surface concentration of active material at cathode reaches its maximum value, the discharging rate cannot exceed the limiting current density owing to diffusion limitations. Then, the equilibrium potential reaches its

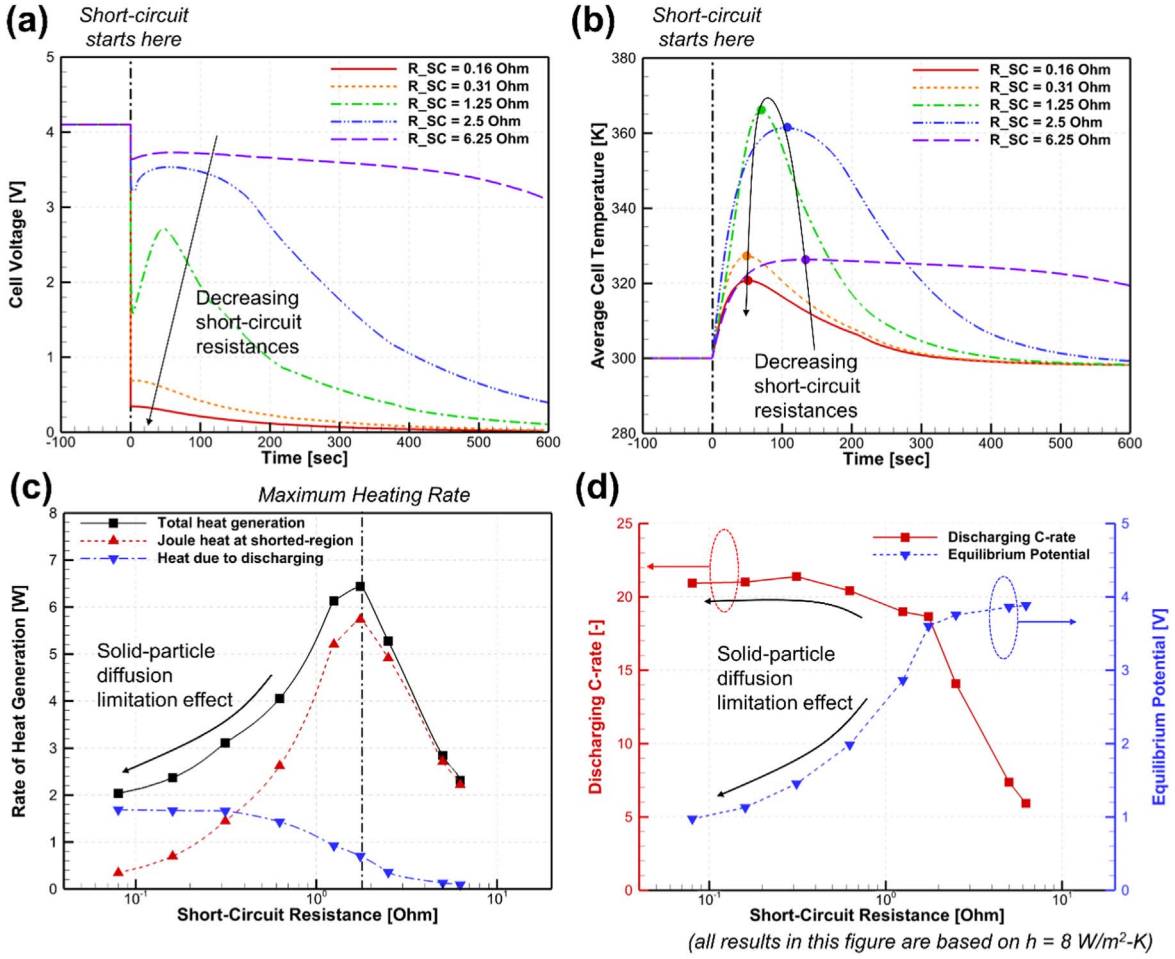

Figure 7. (a) Voltage response at various short-circuit resistances (b) Temperature response at various short-circuit resistances (c) Budget analysis for various heat generation mechanism at various short-circuit resistances (d) Discharging rate and equilibrium potential at various short-circuit resistances (heat transfer coefficient of 8W-m^{-2}K^{-1} is used, data at 90% SOC are selected for Figs. 7c–7d).

minimum value. During discharge, the limiting volumetric current density for anode and cathode are expressed as follows:[31]

$$|j^{Li}|_{an} = a_s F D_s \frac{\overline{c_s}}{l_{se}}\bigg|_{an} \quad [28]$$

$$|j^{Li}|_{ca} = a_s F D_s \frac{c_{s,\max} - \overline{c_s}}{l_{se}}\bigg|_{ca} \quad [29]$$

To illustrate this phenomenon in more detail, in-plane distributions of surface stoichiometries at mid-cathode region (0.00014 m) at 90% average SOC are plotted in Fig. 8a. The stoichiometry is defined as a ratio of temporal Li^+ concentration at the surface of the active material, to its maximum value, which is expressed as:

$$x = \frac{c_s}{c_{\max}} \quad [30]$$

It is clearly seen that, as short circuit resistance decreases, the surface concentration of cathode active material increases due to higher current and converges to its maximum value. The Li^+ concentration at the surface tends to be lower near the shorted region due to higher temperature and hence higher diffusivity. At $R_{SC} = 0.16\Omega$, the stoichiometry reaches almost 1.0 at all region, indicating that the volumetric current density reaches the limiting volumetric current density (Eqs. 28–29) and hence the transport of active material is strongly limited by diffusion.

The in-plane non-uniformity in transport gradually vanishes with decreasing short-circuit resistance as the fraction of heating rate at the shorted region gradually decreases. Figure 8b illustrates the in-plane distribution of local SOC (obtained by volume averaging the stoichiometry shown in Eq. 30 across the active material particle at a given location) at various short-circuit resistance, at 90% of the SOC averaged across the cell. As discussed in the last section, the active material at anode tends to be depleted faster near the shorted-circuit region due to higher temperature. However, as the heating regime being shifted to "global regime" from "local regime" with decreasing short-circuit resistance, the distribution of local SOC becomes progressively more uniform along the in-plane direction. Figure 9 describes the time evolution of the concentration of Li + in electrolyte with its flux for $R_{SC} = 0.16\Omega$. Compared to Fig. 6 ($R_{SC} = 2.5\Omega$), the distributions of c_e as well as the flux of Li + in electrolyte are much more uniform along in-plane direction, as the heating of the cell is relatively more dominated by the cell internal heating. At these very low resistance shorting cases, the discharging rate as well as the heat generation rate is limited by diffusion of Li^+ within the active material, which serves as a origin of cell internal heat generation. Per earlier discussions on Fig. 7, the concentration profiles (and hence temperature distribution) are uniform as a function of distance from the short, across the area of the cell. In other words, the short-circuit has evolved from being "local" (Fig. 6) to "global" (Fig. 9).

Thus, tailoring the transport of lithium within in active materials during an internal short-circuit, can provide insights into managing the onset of thermal runaway reactions: for instance, the binder

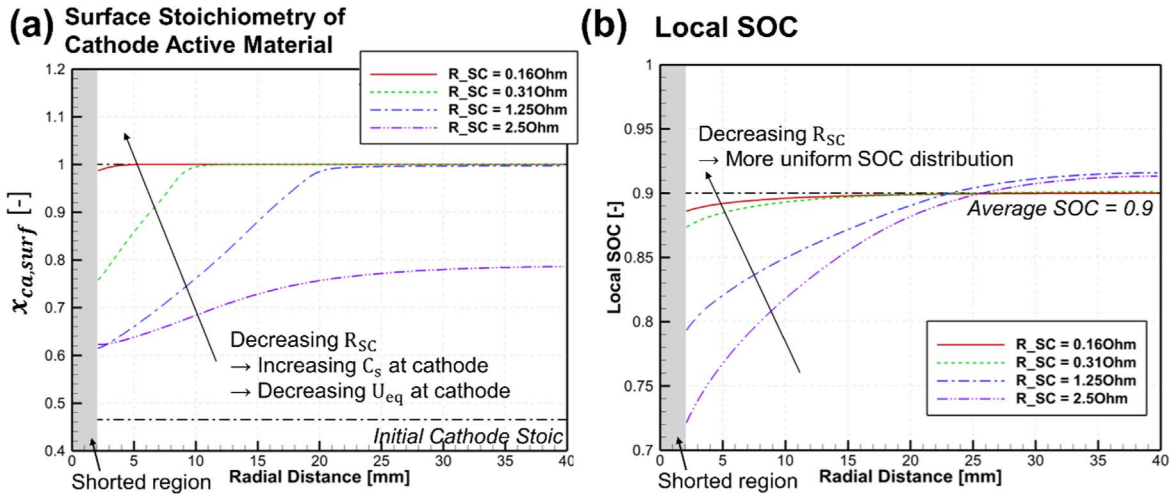

Figure 8. Distribution of (a) local stoichiometry at surface of active material at mid-cathode (b) local state-of-charge at mid-anode (heat transfer coefficient of 8W-m^{-2}K^{-1} is used, data at 90% SOC are selected.

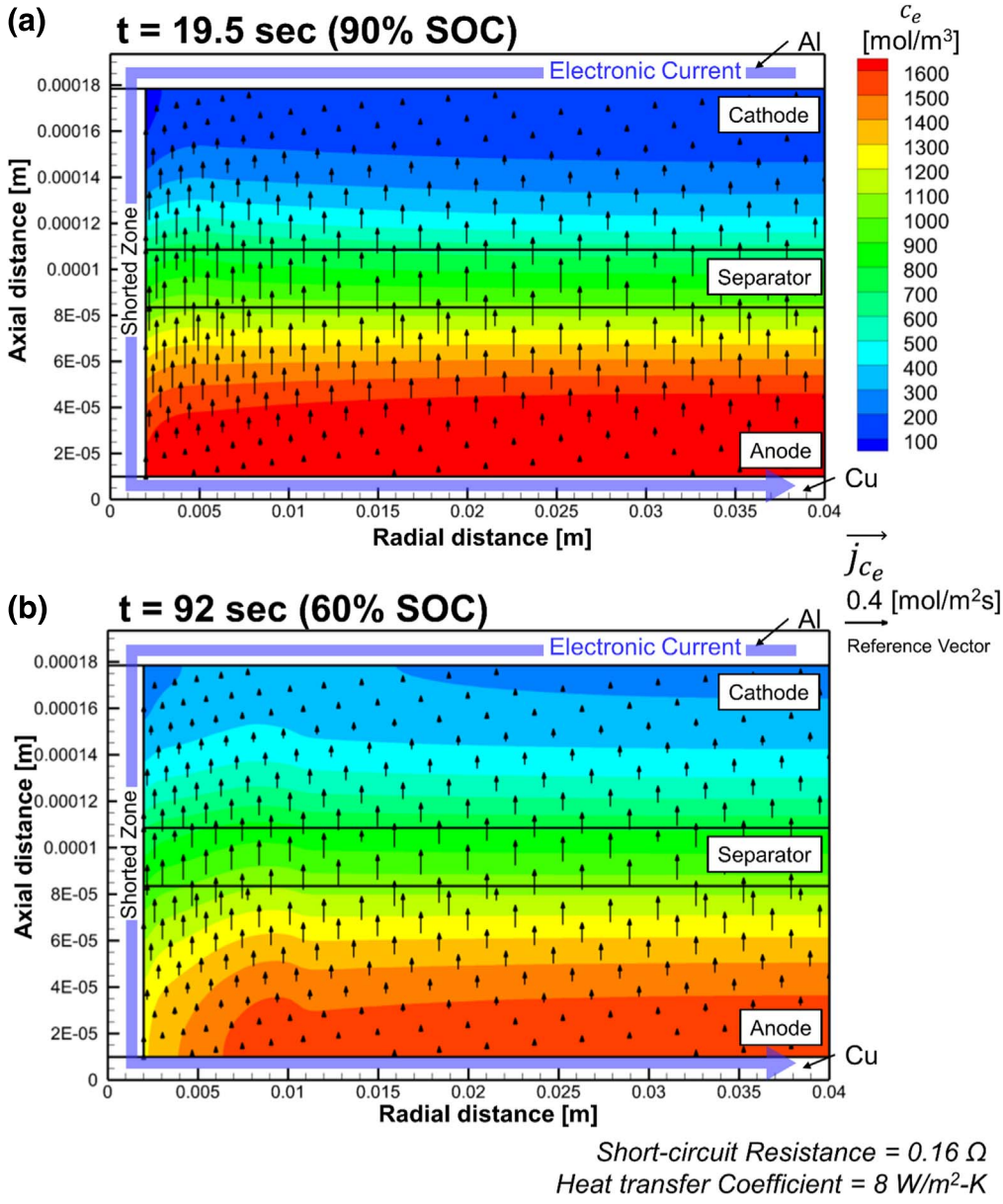

Figure 9. Time evolution of Li+ concentration in electrolyte and diffusion flux of Li+ in electrolyte at (a) 19.5 s (90% SOC), (b) 92 s (60% SOC).

recipe or coatings on the current collectors in some commercial cell designs enable isolation of the active material at higher temperatures, thus containing the diffusion of Li^+ ions.

Finally, it is also important to characterize the criterion for the transition from a local to a global heating regime. As already described in this work as well as previous studies,[17,30] as short-circuit resistance decreases, heating regime progressively shifts to "global heating regime". Therefore, the regime shift is strongly related to the ratio between the cell resistance and the short-circuit resistance. In our analysis, the cell resistance is found to be $0.3 \sim 0.5\ \Omega$ based on the below equation:

$$R_{cell} = \frac{Q_{cell,\text{internal}}}{I^2} \quad [31]$$

where the heat generation rate can be found from Fig. 8c. Considering that the heat generation in a cell due to electrochemical reaction ($Q_{cell,EC}$) is dominant when the short-circuit resistance is below $0.1\ \Omega$ (17% at $R_{SC} = 0.08\Omega$), for the parameters used in this study, at a threshold of:

$$\left.\frac{R_{cell}}{R_{SC}}\right|_{th} = 4 \quad [32]$$

we observer this transition. For example, if the ratio of the cell resistance to the short-circuit resistance is larger than 4, the "global heating" is dominant mechanism for heating of battery during the short-circuit.

Conclusions

In this work, we numerically analyzed the evolution of physical states during an internal short-circuit event for different short-circuit resistances and thermal conditions, using a coupled electrochemical-thermal model. First, electrochemical behavior at different thermal conditions were investigated. During an ISC, transport and kinetics are greatly influenced by the cooling conditions. It is also found that temperature tends to be higher near the shorted-region due to Joule heating, which promotes electrochemical reactions nearby and hence causes in-plane non-uniformities.

Second, electrochemical and thermal behavior under a wide range of short-circuit resistances are analyzed. As the short-circuit resistance decreases, the discharging current increases and converges to the limiting charging current, owing to limitations in Li^+ diffusion within the solid particles. This solid-particle diffusion limitation causes a decrease in equilibrium potential and hence decrease of cell potential, which results in the decrease of Joule heating at the shorted region. This contributes to the shift of heating regime from "local heating" to "global heating". Owing to this regime shift, more uniform electrochemical reaction rates as well as more uniform distribution of Li^+ in electrolyte are observed along in-plane direction. Based on this analysis, we suggest development of a threshold ratio (in our case, 4.0) of the internal cell resistance to the short-circuit resistance that tells us when the "global heating" becomes dominant.

It should be noted that the current numerical methodology does not explicitly model thermal abuse reactions such as SEI breakdown, reformations and electrolyte decomposition. This may result in an under-estimation of temperature rise[11] or over-estimation of electrochemical reaction rate after the local temperature reaches the onset temperature of thermal runaway. While inclusion of these phenomena will likely change the value of the threshold ratio, the process used to analyze a short circuit, and recommendations to calculate the ratio remain valid due to the wide range of values chosen for the parameter R_{SC}. These values were chosen to serve as bounds for the best and worst case outcome for the thermal response. In future studies, the role of thermal abuse reactions on thermal and electrochemical behavior in the electrode-level will be addressed by implementing the current numerical framework.

Acknowledgments

This study was supported by the Vehicle Technologies Office, Office of Energy Efficiency and Renewable Energy, U.S. Department of Energy under contact number WBS1.1.2.406. The research was performed using computational resources sponsored by the Department of Energy's Office of Energy Efficiency and Renewable Energy, located at the National Renewable Energy Laboratory. The U.S. Government retains and the publisher, by accepting the article for publication, acknowledges that the U.S. Government retains a nonexclusive, paid up, irrevocable, worldwide license to publish or reproduce the published form of this work, or allow others to do so, for U.S. Government purposes.

ORCID

Jinyong Kim https://orcid.org/0000-0002-9540-2197

References

1. D. B. Richardson, *Renew. Sustain. Energy Rev.*, **19**, 247 (2013).
2. T. D. Hatchard, D. D. MacNeil, A. Basu, and J. R. Dahn, *J. Electrochem. Soc.*, **148**, A761 (2001).
3. G. H. Kim, A. Pesaran, and R. Spotnitz, *J. Power Sources*, **170**, 476 (2007).
4. B. Liu et al., *Energy Storage Mater.*, **24**, 85 (2019).
5. S. Abada et al., *J. Power Sources*, **306**, 178 (2016).
6. J. Deng et al., *Safety Modeling of Lithium-ion Batteries under Mechanical Abuse*, 11 (2018), https://dynalook.com/conferences/15th-international-ls-dyna-conference/electromagnetics/safety-modeling-of-lithium-ion-batteries-under-mechanical-abuse.
7. L. Lu, X. Han, J. Li, J. Hua, and M. Ouyang, *J. Power Sources*, **226**, 272 (2013).
8. J. Lamb, C. J. Orendorff, E. P. Roth, and J. Langendorf, *J. Electrochem. Soc.*, **162**, 2131 (2015).
9. R. C. Shurtz et al., *J. Electrochem. Soc.*, **166**, A2498 (2019).
10. T. G. Zavalis, M. Behm, and G. Lindbergh, *J. Electrochem. Soc.*, **159**, 848 (2012).
11. W. Zhao, G. Luo, and C. Y. Wang, *J. Electrochem. Soc.*, **162**, 207 (2015).
12. C. Zhang, S. Santhanagopalan, M. A. Sprague, and A. A. Pesaran, *J. Power Sources*, **290**, 102 (2015).
13. J. Deng et al., *Safety Modeling of Lithium-ion Batteries under Mechanical Abuse, Presented at the 15th International LS-DYNA(R) Users Conference*, Detroit, June 10-12 (2018), https://dynalook.com/conferences/15th-international-ls-dyna-conference/electromagnetics/safety-modeling-of-lithium-ion-batteries-under-mechanical-abuse.
14. J. Marcicki et al., *J. Electrochem. Soc.*, **164**, A6440 (2017).
15. C. Zhang, S. Santhanagopalan, M. A. Sprague, and A. A. Pesaran, *ECS Trans.*, **72**, 9 (2016).
16. W. Zhao, G. Luo, and C. Wang, *J. Electrochem. Soc.*, **162**, 1352 (2015).
17. W. Fang, P. Ramadass, and Z. Zhang, *J. Power Sources*, **248**, 1090 (2014).
18. R. Zhao, J. Liu, and J. Gu, *Appl. Energy*, **173**, 29 (2016).
19. S. Santhanagopalan, P. Ramadass, and J. (Zhengming) Zhang, *J. Power Sources*, **194**, 550 (2009).
20. https://gtisoft.com/gt-autolion/.
21. W. B. Gu and C. Y. Wang, *ECS Proc.*, **99**, 748 (2000).
22. K. Smith and C. Y. Wang, *J. Power Sources*, **161**, 628 (2006).
23. M. Doyle, J. Newman, A. S. Gozdz, C. N. Schmutz, and J. M. Tarascon, *J. Electrochem. Soc.*, **143**, 1890 (1996).
24. M. Keyser et al., *J. Power Sources*, **367**, 228 (2017).
25. S. K. Rahimian, S. Rayman, and R. E. White, *J. Power Sources*, **224**, 180 (2013).
26. https://ansys.com/products/fluids/ansys-fluent.
27. S. V. Patankar, *Numerical Heat Transfer and Fluid Flow* (Hemisphere Publishing Corp, New York) (1980).
28. L. O. Valøen and J. N. Reimers, *J. Electrochem. Soc.*, 882 (2005).
29. P. Ramadass, B. Haran, P. M. Gomadam, R. White, and B. N. Popov, *J. Electrochem. Soc.*, **151**, A196 (2004).
30. G.-H. Kim, K. Smith, and A. Pesaran, *Lithium-Ion Battery Safety Study Using Multi-Physics Internal Short-Circuit Model*, *Presented at The 5th International Symposium on Large Lithium-Ion Battery Technology and Application in Conjunction with AABC09*, Long Beach, CA., 9–10 June 2009 (2009), http://osti.gov/bridge/servlets/purl/958001-w3oPeY/.
31. J. Mao, W. Tiedemann, and J. Newman, *J. Power Sources*, **271**, 444 (2014).